



Investigation of the structure, acidity, and catalytic performance of CuO/Ti_{0.95}Ce_{0.05}O₂ catalyst for the selective catalytic reduction of NO by NH₃ at low temperature

Xiaojiang Yao^{a,b}, Lei Zhang^{a,b}, Lulu Li^{a,b}, Lichen Liu^{a,b}, Yuan Cao^{a,b}, Xian Dong^c, Fei Gao^b, Yu Deng^b, Changjin Tang^{a,b,*}, Zhuo Chen^c, Lin Dong^{a,b,*}, Yi Chen^{a,b}

^a Key Laboratory of Mesoscopic Chemistry of MOE, School of Chemistry and Chemical Engineering, Nanjing University, Nanjing 210093, PR China

^b Jiangsu Key Laboratory of Vehicle Emissions Control, Center of Modern Analysis, Nanjing University, Nanjing 210093, PR China

^c School of Chemistry and Material Science, Guizhou Normal University, Guiyang 550001, PR China

ARTICLE INFO

Article history:

Received 15 August 2013

Received in revised form 3 December 2013

Accepted 6 December 2013

Available online 25 December 2013

Keywords:

CuO/Ti_{0.95}Ce_{0.05}O₂ catalyst

Coordination structure

Electron interaction

Surface acidity

NH₃-SCR model reaction

ABSTRACT

Anatase TiO₂, Ti_{0.95}Ce_{0.05}O₂ solid solution, and CeO₂ were synthesized by inverse co-precipitation method, and then used as supports to prepare CuO/TiO₂, CuO/Ti_{0.95}Ce_{0.05}O₂, and CuO/CeO₂ catalysts through incipient-wetness impregnation method. The obtained samples were investigated in detail by means of N₂-physisorption, XRD, LRS, H₂-TPR, XPS, NH₃-TPD, and *in situ* DRIFTS technologies. Furthermore, NH₃-SCR of NO in the presence of excess oxygen was chosen as a model reaction to evaluate the catalytic performances of these samples. The obtained results indicate that the incorporation of Ce⁴⁺ into the lattice of anatase TiO₂ leads to the formation of unstable distorted octahedral coordination structure of Cu²⁺ in CuO/Ti_{0.95}Ce_{0.05}O₂ catalyst and the enhancement of the electron interaction between copper oxide species and Ti_{0.95}Ce_{0.05}O₂ support through the redox cycles of Cu²⁺ + Ce³⁺ ↔ Cu⁺ + Ce⁴⁺ and Cu²⁺ + Ti³⁺ ↔ Cu⁺ + Ti⁴⁺, which are beneficial to the formation of more Lewis acid sites on the surface of CuO/Ti_{0.95}Ce_{0.05}O₂ catalyst and the activation of reactant molecules to generate more NH₄NO₂ species, all of these may promote the enhancement of catalytic performance for NH₃-SCR of NO in the presence of excess oxygen. Finally, a possible reaction mechanism (schematic diagram) is tentatively proposed to further understand this model reaction.

© 2013 Elsevier B.V. All rights reserved.

1. Introduction

With the enhancement of people's environmental protection awareness and the gradual rigor of worldwide regulations, atmosphere contamination treatment attracts much attention of the researchers. Nitrogen oxides (NO_x) as one of the main atmosphere pollutants are emitted from stationary sources (e.g., coal-fired power plants) and mobile sources (e.g., vehicle exhausts), which not only cause the photochemical smog and acid rain, but also induce the ozone depletion and greenhouse effect [1–3]. As a result, the elimination of NO_x emitted from coal-fired power plants and vehicle exhausts becomes a research hotspot in recent years. Many potential denitrification techniques (such as selective catalytic reduction, pulse corona plasma, storage reduction, electron beam irradiation, and microwave method, etc.) have been explored to

reduce the emission of NO_x [1,4]. Among these denitrification techniques, the selective catalytic reduction of NO_x by NH₃ (NH₃-SCR) has been proved to be the most chemically efficient and cost-effective technology to remove NO_x from coal-fired flue gas, and the general NH₃-SCR reaction is: 4NO + 4NH₃ + O₂ = 4N₂ + 6H₂O [5–7]. The commercialized industrial catalysts for this reaction are V₂O₅-WO₃(MoO₃)/TiO₂, which exhibit excellent catalytic performance in the temperature range of 300–400 °C. However, there are still some disadvantages in these catalyst systems, such as [8–10]: (1) V₂O₅ is easy to sublime and shed in the using process, and further generates biological toxicity when it enters into the environment; (2) the operation temperature window is relatively narrow, the low-temperature activity is unsatisfactory, and a large number of N₂O will form at high temperature; (3) the high-temperature thermal stability is very poor. As a result, many efforts have been made to develop novel non-vanadium-based metal oxide denitrification catalysts with merits of high efficiency, low cost, and environment friendly.

In recent investigations, many support materials (TiO₂, CeO₂, Al₂O₃, and ZrO₂, etc.) have been widely used for NH₃-SCR reaction [11–14]. Among these metal oxides, anatase TiO₂ is the most

* Corresponding authors at: School of Chemistry and Chemical Engineering, Nanjing University, Hankou Road 22#, Nanjing, Jiangsu 210093, PR China. Tel.: +86 25 83592290; fax: +86 25 83317761.

E-mail addresses: tangcj@nju.edu.cn (C. Tang), donglin@nju.edu.cn (L. Dong).

favorable one due to its excellent resistance performance to SO_2 poisoning [15]. However, the application of pure anatase TiO_2 is highly discouraged because of the poor mechanical strength, low BET specific surface area, and the transformation to rutile TiO_2 during operation at high temperature [16,17]. With the purpose of overcoming these disadvantages, many metal cations (Ce^{4+} , Zr^{4+} , and Sn^{4+} , etc.) are normally incorporated into the lattice of anatase TiO_2 and have been studied systematically [1,8,16,17]. Ceria has been attracting much attention in NH_3 -SCR reaction due to the advantages of the excellent redox property, empty d-electron orbital, and the high oxygen storage/release capacity associated with the formation of oxygen vacancy [1,5]. Copper-based catalysts are commonly considered as the potential candidates of vanadium-based catalysts for NH_3 -SCR reaction because of the good low-temperature activity, non-toxicity, and low cost [18,19]. As a result, the combination of anatase TiO_2 , CeO_2 , and CuO is bound to exhibit good resistance performance to SO_2 poisoning, high hydrothermal stability, and excellent catalytic performance for NH_3 -SCR reaction.

It is widely reported that the catalytic performances of copper-based catalysts for NH_3 -SCR reaction are closely related to the texture and dispersion of copper oxide species, which are significantly influenced by the supports [18–21]. Furthermore, Liu et al. pointed out that the synergistic effect of the dual redox cycles ($\text{Cu}^{2+} + \text{Ce}^{3+} \leftrightarrow \text{Cu}^+ + \text{Ce}^{4+}$ and $\text{Cu}^{2+} + \text{Ti}^{3+} \leftrightarrow \text{Cu}^+ + \text{Ti}^{4+}$) is beneficial to the enhancement of the catalytic performance for NH_3 -SCR reaction [22]. However, the details of the relationship among the “composition–structure–property” are still not very clear. Therefore, in the present work, anatase TiO_2 , $\text{Ti}_{0.95}\text{Ce}_{0.05}\text{O}_2$ solid solution, and CeO_2 were synthesized by inverse co-precipitation method, and then used as supports to prepare copper-based catalysts. The obtained samples were characterized by means of N_2 -physisorption, XRD, LRS, H_2 -TPR, XPS, NH_3 -TPD, and *in situ* DRIFTS technologies. Moreover, “ $\text{NO} + \text{NH}_3 + \text{O}_2$ ” as a model reaction was carried out to evaluate the catalytic performances of these samples. This study is mainly focused on: (1) exploring the influence of incorporating Ce^{4+} into anatase TiO_2 lattice on the coordination structure, surface acidity, and catalytic performance of $\text{CuO}/\text{Ti}_{0.95}\text{Ce}_{0.05}\text{O}_2$ catalyst to further understand the relationship among the “composition–structure–property”; (2) investigating the interaction of NH_3 and $\text{NO} + \text{O}_2$ with these copper-based catalysts by *in situ* DRIFTS technique in the temperature range of 25–400 °C.

2. Experimental

2.1. Catalysts preparation

The $\text{Ti}_{0.95}\text{Ce}_{0.05}\text{O}_2$ solid solution (Ti:Ce = 19:1 mole ratio) was synthesized by inverse co-precipitation method [2]. Briefly, the desired amounts of titanium (IV) tetrachloride and ammonium cerium (IV) nitrate were dissolved in distilled water separately and mixed together for magnetic stirring 2 h, and then added dropwisely into the excess ammonia (25%) with vigorously stirring until pH = 10. The resulting suspension was kept in stirring for another 3 h, aged 24 h, and then filtered, washed several times with distilled water until no pH changed and no Cl^- detected by the solution of AgNO_3 . The obtained cake was oven dried at 110 °C for 12 h and finally calcined in the flowing air at 500 °C for 5 h. For simplicity, the synthesized sample is denoted as TC, and its BET specific surface area is $107.8 \text{ m}^2 \text{ g}^{-1}$. Moreover, anatase TiO_2 and CeO_2 were prepared by a similar way for comparison, whereas their BET specific surface areas are only 66.1 and $46.1 \text{ m}^2 \text{ g}^{-1}$ respectively.

The xCuO/TC samples were prepared by incipient-wetness impregnating the TC support with $\text{Cu}(\text{CH}_3\text{COO})_2$ solution, where

x indicates the loading amount of copper oxide (e.g., $0.08\text{CuO}/\text{TC}$ catalyst represents the CuO loading amount is $0.8 \text{ mmol Cu}^{2+}/100 \text{ m}^2$ TC). The mixture was kept in stirring for 2 h and evaporated to remove the water at 100 °C during the oil bath. The obtained materials were oven dried at 110 °C for 12 h, and then calcined in the flowing air at 450 °C for 4 h. Furthermore, $0.08\text{CuO}/\text{TiO}_2$ and $0.08\text{CuO}/\text{CeO}_2$ catalysts were also prepared by the same method for comparison.

2.2. Catalysts characterization

Textural characteristics of these supports were measured by N_2 -physisorption at -196°C on a Micromeritics ASAP-2020 analyzer, using the Brunauer–Emmett–Teller (BET) method to determine their specific surface areas. Prior to each analysis, the sample was degassed under vacuum at 300 °C for 4 h.

X-ray diffraction (XRD) patterns were recorded on a Philips X'pert Pro diffractometer using Ni-filtered $\text{Cu K}\alpha$ radiation ($\lambda = 0.15418 \text{ nm}$). The X-ray tube was operated at 40 kV and 40 mA. The intensity data were collected in a 2θ range of 10° – 80° . The scan speed was set at $10^\circ \text{ min}^{-1}$ with a step size of 0.02° . The mean crystallite sizes (D_β) from the strongest peak of these samples were determined by Debye–Scherrer equation ($D_\beta = K\lambda/\beta\cos\theta$), where K is the particle shape factor, usually taken as 0.89, λ is the X-ray wavelength, β is the full-width at half maximum height (FWHM) in radians, and θ is the diffraction angle.

Laser Raman spectra (LRS) were collected on a Renishaw inVia Laser Raman spectrometer using Ar^+ laser beam. The Raman spectra were recorded with an excitation wavelength of 514 nm and the laser power of 20 mW.

H_2 -temperature programmed reduction (H_2 -TPR) experiments were performed in a quartz U-type reactor connected to a thermal conductivity detector (TCD) with Ar-H_2 mixture (7.0% of H_2 by volume, 70 ml min^{-1}) as a reductant. Prior to the reduction, the sample (50 mg) was pretreated in a high purified N_2 stream at 300 °C for 1 h and then cooled to room temperature. After that, the TPR started from 50 °C to target temperature at a rate of $10^\circ\text{C min}^{-1}$.

X-ray photoelectron spectra (XPS) were performed on a PHI 5000 VersaProbe system, using monochromatic $\text{Al K}\alpha$ radiation (1486.6 eV) operating at an accelerating power of 15 kW. Before the measurement, the sample was outgassed at room temperature in a UHV chamber ($<5 \times 10^{-7} \text{ Pa}$). The sample charging effects were compensated by calibrating all binding energies (BE) with the adventitious C 1s peak at 284.6 eV. This reference gave BE values with accuracy at $\pm 0.1 \text{ eV}$.

NH_3 -temperature programmed desorption (NH_3 -TPD) experiments were carried out on a multifunction chemisorption analyzer with a quartz U-tube reactor, detected by a thermal conductivity detector (TCD). About 100 mg of the sample was pretreated by passage of high purified He (40 ml min^{-1}) at 450 °C for 1 h. After pretreatment, the sample was saturated with high purified NH_3 (40 ml min^{-1}) at 100 °C for 1 h and subsequently flushed with the flowing high purified He (40 ml min^{-1}) at the same temperature for 1 h to remove gaseous and weakly adsorbed NH_3 , then the sample was heated to 900 °C at a rate of $10^\circ\text{C min}^{-1}$ in the flowing high purified He (40 ml min^{-1}).

In situ diffuse reflectance infrared Fourier transform spectra (*in situ* DRIFTS) were collected from 650 to 4000 cm^{-1} at a spectral resolution of 4 cm^{-1} (number of scans, 32) on a Nicolet 5700 FT-IR spectrometer equipped with a high-sensitive MCT detector cooled by liquid N_2 . The DRIFTS cell (Harrick) was fitted with a ZnSe window and a heating cartridge that allowed sample to be heated to 400 °C. The fine catalyst powder placed on a sample holder was carefully flattened to enhance IR reflection. The sample was pretreated with a high purified N_2 stream at 400 °C for 1 h to eliminate the physisorbed water and other impurities. The

sample background of each target temperature was collected during the cooling process. At ambient temperature, the sample was exposed to a controlled stream of $\text{NH}_3\text{-N}_2$ (1% of NH_3 by volume) or $\text{NO-N}_2 + \text{O}_2\text{-N}_2$ (1% of NO and 5% of O_2 by volume) at a rate of 50 ml min^{-1} for 1 h to be saturated. And then, the gaseous and weakly adsorbed NH_3 molecules were purged by a high purified N_2 stream (50 ml min^{-1}) for 1 h. Desorption/reaction studies were performed by heating the adsorbed species and the spectra were recorded at various target temperatures at a rate of $10^\circ\text{C min}^{-1}$ from room temperature to 400°C (in the flowing high purified N_2 stream for NH_3 -adsorption, whereas in the $\text{NO-N}_2 + \text{O}_2\text{-N}_2$ (1% of NO and 5% of O_2 by volume) stream for $\text{NO} + \text{O}_2$ -adsorption) by subtraction of the corresponding background reference.

2.3. Catalytic performance measurements

The catalytic performances of these samples for the selective catalytic reduction of NO by NH_3 ($\text{NH}_3\text{-SCR}$) in the presence of excess oxygen were determined under steady state, involving a feed stream with a fixed composition, 500 ppm NO , 500 ppm NH_3 , 5% O_2 , 100 ppm SO_2 (when used), 5% H_2O (when used), and N_2 in balance. The sample (50 mg) was fitted in a quartz tube and pretreated in a high purified N_2 stream at 300°C for 1 h and then cooled to room temperature, after that, the mixed gases were switched on. The reactions were carried out at different temperatures with a space velocity of $120,000\text{ ml g}^{-1}\text{ h}^{-1}$. The concentrations of NO , NH_3 , NO_2 , and N_2O were measured at 150°C by a Thermofisher IS10 FTIR spectrometer equipped with a 2 m path-length gas cell (250 ml volume). The gas path from the reactor to FTIR spectrometer was kept a fixed temperature of 150°C to avoid the deposition of $\text{NH}_4\text{NO}_2/\text{NH}_4\text{NO}_3$ and the dissolution of NH_3 in liquid H_2O . The NO conversion and N_2 selectivity were calculated from the following equations:

$$\text{NO conversion (\%)} = \frac{[\text{NO}]_{\text{in}} - [\text{NO}]_{\text{out}}}{[\text{NO}]_{\text{in}}} \times 100 \quad (1)$$

$$\text{N}_2 \text{ selectivity (\%)} = \frac{[\text{NO}]_{\text{in}} - [\text{NO}]_{\text{out}} + [\text{NH}_3]_{\text{in}} - [\text{NH}_3]_{\text{out}} - [\text{NO}_2]_{\text{out}} - 2[\text{N}_2\text{O}]_{\text{out}}}{[\text{NO}]_{\text{in}} - [\text{NO}]_{\text{out}} + [\text{NH}_3]_{\text{in}} - [\text{NH}_3]_{\text{out}}} \times 100 \quad (2)$$

3. Results and discussion

3.1. Structural characteristics (XRD and LRS)

The XRD results of the obtained samples are displayed in Fig. 1. It can be seen from Fig. 1a that the pure TiO_2 exhibits several characteristic diffraction peaks assigned to anatase TiO_2 [PDF-ICDD 21-1272], pure CeO_2 shows a cubic fluorite-type structure [PDF-ICDD 34-0394], while only the broad diffraction peaks attributed to anatase TiO_2 can be observed in the XRD pattern of TC. The characteristic lines corresponding to cubic fluorite-type CeO_2 are absent, and the diffraction peaks of TC shift to low-angle direction slightly compared with anatase TiO_2 (seeing the inserted partial enlarged view in Fig. 1a), which suggest that Ce^{4+} has been successfully incorporated into the lattice of anatase TiO_2 to form uniform solid solution maintaining the anatase crystal form [8,23]. We can notice that the diffraction peaks of TC are broader than those of anatase TiO_2 owing to the decrease of crystallite size (Table 1), which indicates that the introduction of Ce^{4+} into the lattice of anatase TiO_2 may inhibit its grain growth [23]. Moreover, Table 1 shows that the lattice parameter of TC is larger than that of anatase TiO_2 in the *c* direction, which is mainly because of the fact that the ionic radius of Ce^{4+} (0.92 Å) is larger than that of Ti^{4+} (0.68 Å), and the incorporation of Ce^{4+} into the lattice of anatase TiO_2 results in the expansion and distortion of the lattice [1,23]. Interestingly, it can be noted from Table 1 that the BET specific surface area of TC ($107.8\text{ m}^2\text{ g}^{-1}$) is obviously larger than that of anatase TiO_2 ($66.1\text{ m}^2\text{ g}^{-1}$) and CeO_2

($46.1\text{ m}^2\text{ g}^{-1}$), which suggests that the incorporation of Ce^{4+} into the lattice of anatase TiO_2 can improve its texture property effectively.

Fig. 1b exhibits the XRD patterns of a series of xCuO/TC samples. For the samples with low CuO loading amount ($<1.2\text{ mmol Cu}^{2+}/100\text{ m}^2\text{ TC}$), no diffraction peaks of crystalline CuO [PDF-ICDD 48-1548] can be detected, which indicates that the copper oxide species are in the forms of highly dispersed state or/and clustered state on the surface of TC support. When the CuO loading amount reaches $1.2\text{ mmol Cu}^{2+}/100\text{ m}^2\text{ TC}$, the diffraction peaks of crystalline CuO appear at 35.5 and 38.7° , and the intensities of the peaks increase with the increase of CuO loading amount.

With the purpose of further determining the dispersion capacity of CuO on the surface of TC support, XRD quantitative analysis was carried out by calculating the dominant diffraction peak intensity ratios of the crystalline CuO to TC support as a function of copper oxide loading amount, and the corresponding results are presented in Fig. 1c. We can find that the fitting straight line relating to the formation of crystalline CuO does not go through the origin, but cut an intercept on the horizontal axis at a value corresponding to the dispersion capacity of CuO on the surface of TC support. And the quantitative XRD results show that the experimental dispersion capacity of CuO on the surface of TC support is about $1.06\text{ mmol Cu}^{2+}/100\text{ m}^2\text{ TC}$. In order to enhance the persuasiveness of the data, XPS quantitative analysis was performed by a similar way, and the results indicate that the experimental dispersion capacity of CuO on the surface of TC support is about $1.12\text{ mmol Cu}^{2+}/100\text{ m}^2\text{ TC}$ (seeing Fig. S1 in the Supplementary Information), which is approximately equal to the value obtained by XRD quantitative analysis. According to our previous works, the dispersion capacity of CuO on the surface of anatase TiO_2 support has been explained by “Incorporation Model” successfully, and the anatase TiO_2 preferentially exposes (001) crystal plane [24–27]. In the present work, the incorporation of Ce^{4+} into the lattice of anatase TiO_2 does not change its anatase crystal form, so we can assume that TC support still

exposes (001) crystal plane preferentially, Cu^{2+} can incorporate into the vacant sites of this crystal plane and the capping oxygen locates at the top of Cu^{2+} to keep electroneutrality, the schematic diagram is shown in Fig. 2. Based on the “Incorporation Model”, if the (001) crystal plane of TC support is considered as the preferentially exposed plane, the theoretical dispersion capacity of Cu^{2+} on the surface of TC support can be calculated to be $1.16\text{ mmol Cu}^{2+}/100\text{ m}^2\text{ TC}$ (seeing Fig. S2 in the Supplementary Information), which is consistent with the experimental value, so it is reasonable to conclude that Cu^{2+} species are mainly dispersed on the (001) crystal plane of TC support.

It is well known that the supported catalyst with the active component loading amount near the dispersion capacity exhibits the optimal catalytic performance in heterogeneous catalysis. Furthermore, the dispersion capacities of Cu^{2+} on the surface of anatase TiO_2 and CeO_2 are $1.17\text{ mmol Cu}^{2+}/100\text{ m}^2\text{ TiO}_2$ and $1.22\text{ mmol Cu}^{2+}/100\text{ m}^2\text{ CeO}_2$, respectively [26,28]. Therefore, a suitable CuO loading amount ($0.8\text{ mmol Cu}^{2+}/100\text{ m}^2\text{ TiO}_2$ (TC and CeO_2), which is close to their dispersion capacities.) is chosen to carry out a systematic study in the present work, and the corresponding XRD results are shown in Fig. 1d. After the loading of CuO , all of these catalysts keep their original support structure, and no additional diffraction peaks of crystalline CuO can be observed, suggesting that copper oxide species on the surface of these supports are in the forms of highly dispersed state or/and clustered state, which are beyond the detection limit of XRD.

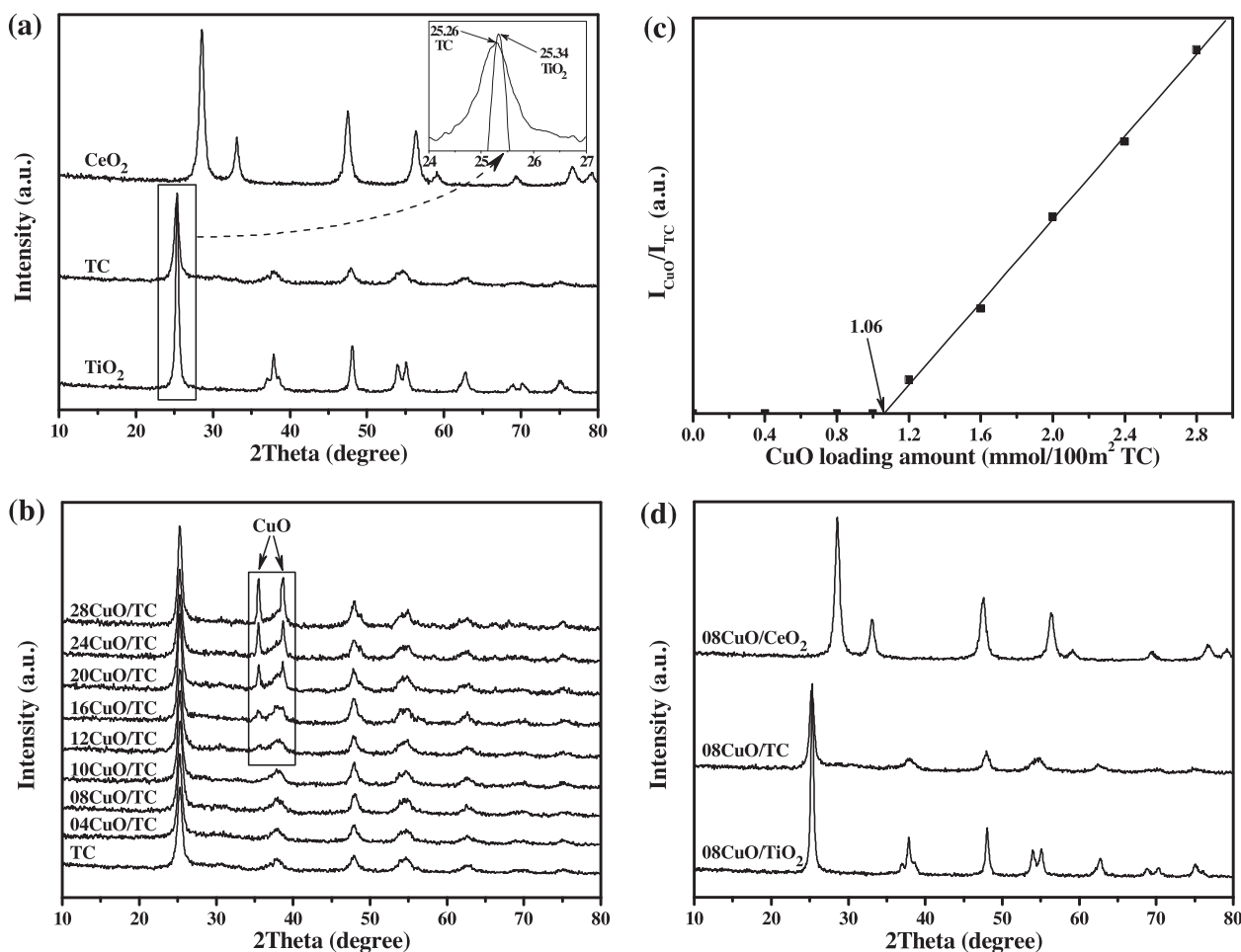


Fig. 1. XRD patterns of the obtained samples: (a) supports, (b) $x\text{CuO/TC}$ samples ($x=0, 04, 08, 10, 12, 16, 20, 24, 28$), (c) the quantitative XRD results of $x\text{CuO/TC}$, and (d) catalysts.

LRS as a complementary surface characterization of XRD is performed on these synthesized samples, and the corresponding results are exhibited in Fig. 3. We can see from Fig. 3a that the pure TiO₂ shows several Raman bands at 144, 195, 394, 514, and 635 cm⁻¹ assigned to the $E_{g(1)}$, $E_{g(2)}$, $B_{1g(1)}$, $A_{1g} + B_{1g(2)}$, and $E_{g(3)}$ vibration modes of anatase TiO₂, respectively [22,29]. Pure CeO₂ exhibits a strong band at 463 cm⁻¹ attributed to the F_{2g} vibration mode of cubic fluorite-type structure [30,31]. However, only the Raman vibration modes of anatase TiO₂ can be detected at the corresponding positions for TC. The Raman band of CeO₂ is absent in TC, and the Raman bands of TC shift to high-wavenumber direction slightly compared with anatase TiO₂, which further confirm that Ce⁴⁺ has been incorporated into the lattice of anatase TiO₂. The Raman results of the copper-based catalysts are presented in Fig. 3b. From this figure, we can find that the Raman bands corresponding to CuO are absent for all the copper-based catalysts, indicating that copper oxide species are in the forms of highly

dispersed state or/and clustered state on the surface of anatase TiO₂, TC, and CeO₂ supports, which is consistent with the results of XRD. In addition, the Raman bands of 08CuO/TiO₂ are very similar with those of anatase TiO₂ without shift, which suggests that the interaction between CuO and anatase TiO₂ is very weak. While the Raman band of 08CuO/CeO₂ shifts to lower wavenumber compared to that of CeO₂ due to the strong interaction between CuO and CeO₂ [32,33]. Interestingly, the Raman bands of 08CuO/TC also shift to low-wavenumber direction slightly compared with TC support, indicating that the incorporation of Ce⁴⁺ into the lattice of anatase TiO₂ may enhance the interaction between Cu²⁺ and Ti⁴⁺.

3.2. Reduction properties (H_2 -TPR)

The reduction properties of the obtained samples are characterized by H_2 -TPR, as shown in Fig. 4. From Fig. 4a, it is obviously that CeO₂ exhibits two reduction peaks at 512 and 788 °C, which are

Table 1
BET surface area, crystallite size, lattice parameter, and the LRS main peak position of the obtained samples.

Samples	BET surface area (m ² g ⁻¹)	Crystallite size (nm)	Lattice parameter (Å)		$E_{g(1)}/F_{2g}$ (cm ⁻¹)
			$a=b$	c	
TiO ₂	66.1	26.8	3.7842	9.4972	144
TC	107.8	21.9	3.7847	9.5124	148
CeO ₂	46.1	18.2	5.4227		463
08CuO/TiO ₂	–	27.5	3.7844	9.4979	144
08CuO/TC	–	22.3	3.7848	9.5132	146
08CuO/CeO ₂	–	19.3	5.4175		459

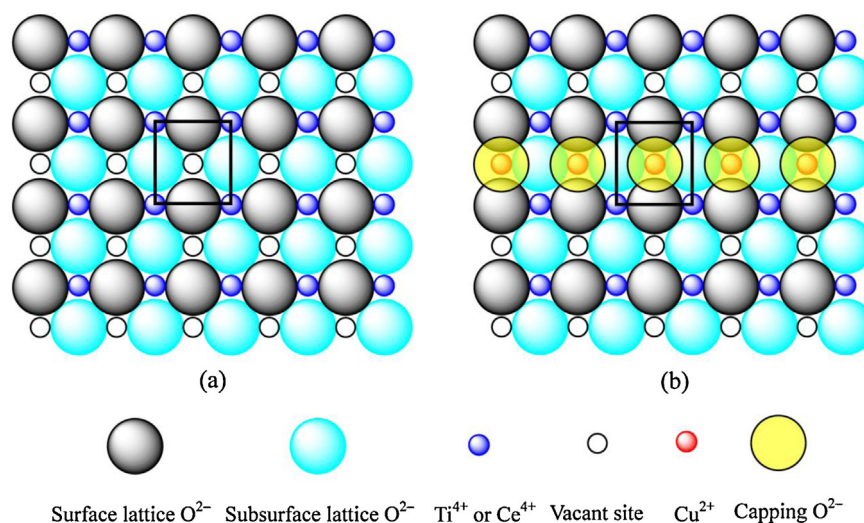


Fig. 2. The schematic diagram of (a) the (001) crystal plane of TC support, and (b) the dispersion of Cu^{2+} on the (001) crystal plane of TC support.

attributed to the reduction of surface CeO_2 and bulk CeO_2 , respectively [9,34]. In a similar way, the two reduction peaks of anatase TiO_2 at 581 and 844 °C can also be assigned to the reduction of surface TiO_2 and bulk TiO_2 , respectively. Interestingly, TC support also shows two reduction peaks, and shifts to low-temperature direction (456 and 584 °C), indicating that the incorporation of Ce^{4+} into the lattice of anatase TiO_2 can promote its reduction efficiently.

H_2 -TPR profiles of $x\text{CuO}/\text{TC}$ samples are presented in Fig. 4b. For the samples with copper oxide loading amount lower than $1.2 \text{ mmol Cu}^{2+}/100 \text{ m}^2$ TC, they exhibit three reduction peaks below 210 °C, and the first two low-temperature reduction peaks (denoted as α and β in Table 2) are attributed to the stepwise reduction of the dispersed copper oxide species, i.e., $\text{Cu}^{2+} \rightarrow \text{Cu}^+$ and $\text{Cu}^+ \rightarrow \text{Cu}^0$, while the third reduction peak (denoted as γ in Table 2) is assigned to the reduction of the clustered CuO [26,33], which is in accordance with the results of XRD. Moreover, with the increase of copper oxide loading amount, the reduction peaks shift to low-temperature direction owing to the hydrogen spill-over effect resulted from the increase of reducible dispersed copper oxide species [35,36]. When the copper oxide loading amount further increases from $1.2 \text{ mmol Cu}^{2+}/100 \text{ m}^2$ TC to $2.8 \text{ mmol Cu}^{2+}/100 \text{ m}^2$ TC, the area of the third reduction peak (γ) begins to increase obviously, indicating that this reduction peak should be related to the reduction of clustered CuO and crystalline CuO according to the XRD results. Especially for $24\text{CuO}/\text{TC}$ and $28\text{CuO}/\text{TC}$ samples, the reduction peaks of β and γ are overlapped due to the increase of crystalline CuO . Furthermore, all the reduction peaks shift to high-temperature direction with the increase of copper oxide loading amount from $1.2 \text{ mmol Cu}^{2+}/100 \text{ m}^2$ TC to $2.8 \text{ mmol Cu}^{2+}/100 \text{ m}^2$ TC. There are two possible reasons: (1) the existence of crystalline CuO inhibits the reduction of dispersed copper oxide species; (2) the crystallite size of crystalline CuO increases with the increase of copper oxide loading amount, which is not conducive to be reduced. Interestingly, we can see from Table 2 that the actual H_2 consumptions of these $x\text{CuO}/\text{TC}$ samples are larger than the corresponding theoretical H_2 consumptions, which suggests that all the

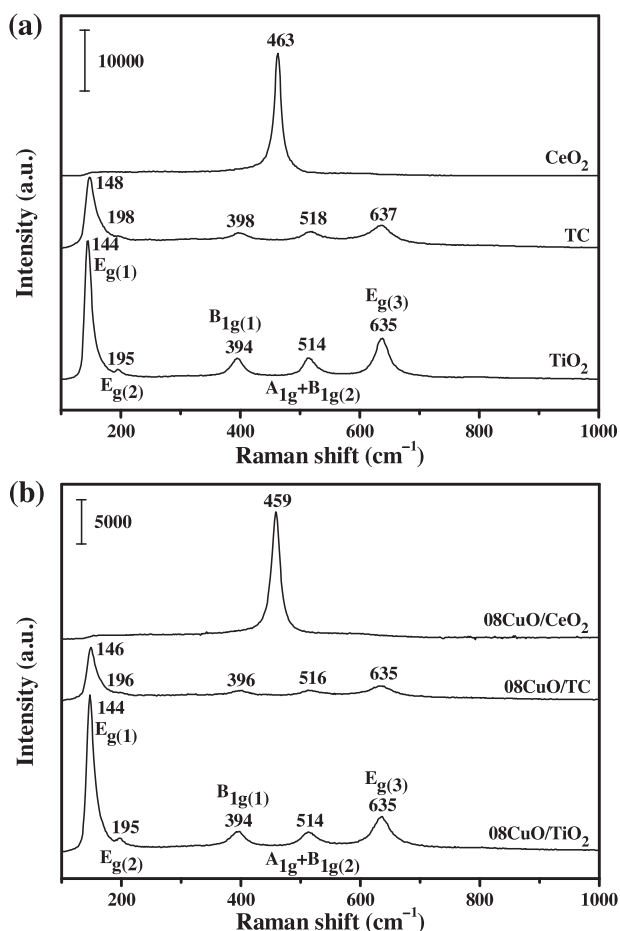


Fig. 3. The LRS results of the obtained samples: (a) supports, and (b) catalysts.

Table 2

The quantitative analysis data of H_2 -TPR over the obtained samples.

Catalysts	Reduction peaks temperature (°C)			The actual H_2 consumption ($\mu\text{mol g}^{-1}$)	The theoretical H_2 consumption ($\mu\text{mol g}^{-1}$)
	α	β	γ		
04CuO/TC	149	172	202	552.7	416.8
08CuO/ TiO_2	163	174	224	504.5	507.3
08CuO/TC	147	164	202	1047.5	806.7
08CuO/ CeO_2	131	158	–	749.4	358.2
10CuO/TC	143	164	201	1123.1	992.4
12CuO/TC	138	178	206	1306.8	1172.3
16CuO/TC	156	197	240	1614.1	1515.7
20CuO/TC	155	196	245	1954.7	1838.8
24CuO/TC	158	–	256	2258.9	2143.5
28CuO/TC	166	–	257	2547.8	2431.3

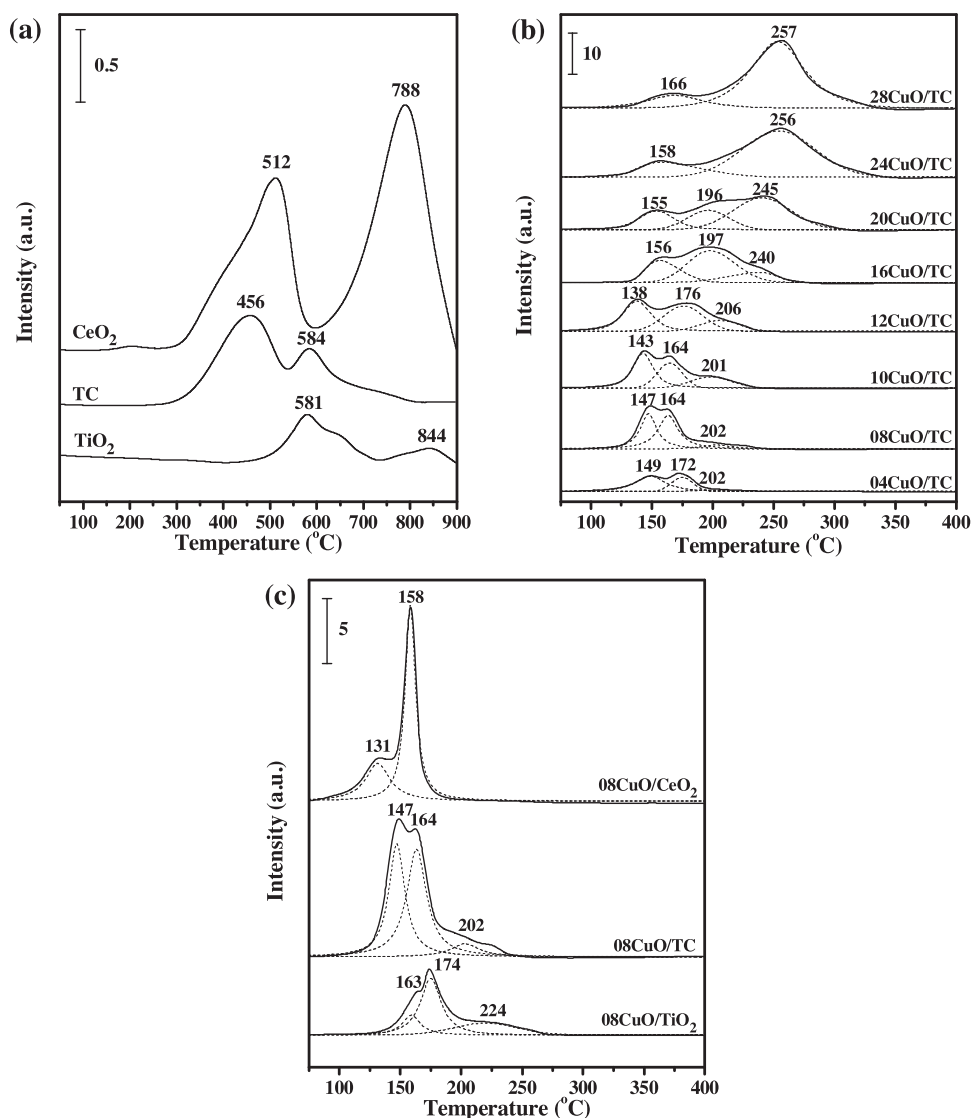


Fig. 4. H₂-TPR profiles of the (a) supports, (b) xCuO/TC samples ($x=04, 08, 10, 12, 16, 20, 24, 28$), and (c) catalysts.

above-mentioned reduction peaks should contain the reduction of TC support. In other words, the loading of copper oxide species can promote the reduction of TC support, and further implying that there are some interaction between copper oxide species and TC support.

Fig. 4c displays the H₂-TPR profiles of 08CuO/TiO₂, 08CuO/TC, and 08CuO/CeO₂ catalysts. From this figure, we can find that the H₂-TPR profile of 08CuO/TiO₂ catalyst is very similar with that of 08CuO/TC catalyst, which also exhibits three reduction peaks at 163, 174, and 224 °C (denoted as α , β , and γ in Table 2) corresponding to stepwise reduction of the dispersed copper oxide species and the reduction of clustered CuO, respectively. However, the reduction peak temperatures of 08CuO/TiO₂ catalyst are obviously higher than those of 08CuO/TC catalyst. The possible reason maybe as follows: It has been reported in our previous publications that the (001) crystal plane is considered as the preferentially exposed crystal plane of anatase TiO₂ [26,27,37]. Furthermore, the above-mentioned discussion of dispersion capacity also indicates that Cu²⁺ species are mainly dispersed on the (001) crystal plane of TC support. Accordingly, the coordination status of Cu²⁺ on the (001) crystal plane of anatase TiO₂ can be drawn as Fig. 5a, we can find that the incorporation of Cu²⁺ into the surface vacant sites of anatase TiO₂ will form a stable octahedral coordination structure.

However, the incorporation of Ce⁴⁺ into the lattice of anatase TiO₂ can change the bond length of Ti–O due to the difference of ionic radii between Ti⁴⁺ (0.68 Å) and Ce⁴⁺ (0.92 Å), which leads to the distortion of the octahedral coordination structure of Cu²⁺, as shown in Fig. 5b. Therefore, Cu²⁺ in 08CuO/TC catalyst can be easier reduced than that in 08CuO/TiO₂ catalyst because that the distorted octahedral coordination structure of Cu²⁺ in the former is more unstable than the stable octahedral coordination structure of Cu²⁺ in the latter. For 08CuO/CeO₂ catalyst, two reduction peaks (denoted as α and β in Table 2) can be observed at 131 and 158 °C, which is also related to the reduction of dispersed copper oxide species. Moreover, the reduction behavior of copper oxide species in 08CuO/CeO₂ catalyst is also influenced by the coordination status of Cu²⁺ [38]. It is well known that CeO₂ exhibits a cubic fluorite structure, and preferentially exposes its (111) crystal plane [39]. Consequently, the schematic diagram of the dispersion of Cu²⁺ on the (111) crystal plane of CeO₂, and the corresponding coordination status of Cu²⁺ are presented in Fig. 6. The incorporation of Cu²⁺ into the surface vacant sites of CeO₂ (111) crystal plane exhibits a trigonal bipyramidal symmetry, which is not as stable as the octahedral coordination structure. Therefore, 08CuO/CeO₂ catalyst can be easier reduced than 08CuO/TiO₂ and 08CuO/TC catalysts. Interestingly, it can be seen from Table 2 that the actual H₂ consumption of 08CuO/TiO₂

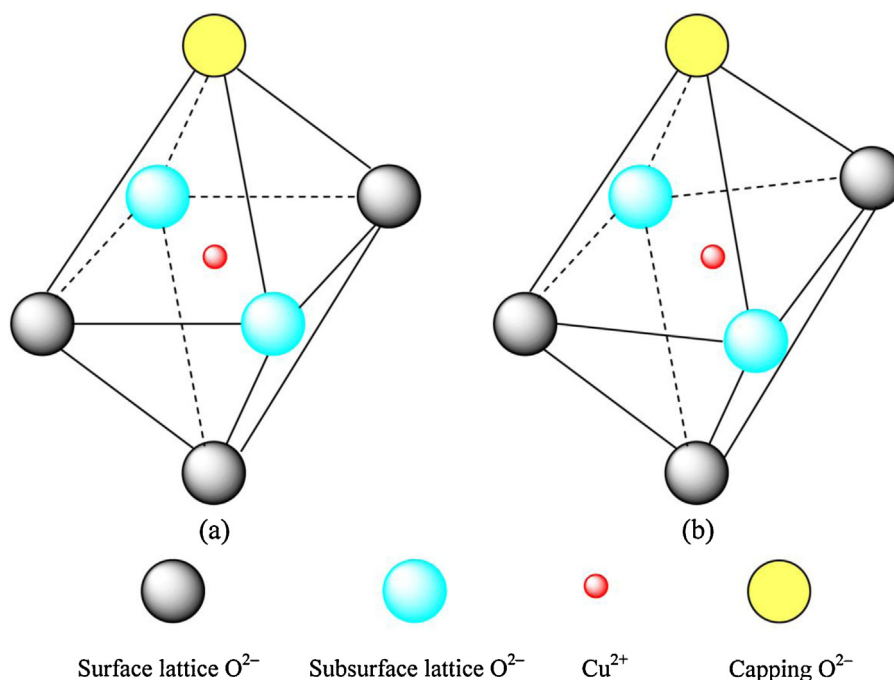


Fig. 5. The schematic model for the coordination status of the dispersed copper oxide species on the (001) crystal plane of (a) anatase TiO_2 , and (b) TC support.

catalyst is close to its theoretical H_2 consumption, which indicates that the interaction between CuO and anatase TiO_2 is too weak to promote the reduction of anatase TiO_2 support. However, the actual H_2 consumptions of 08CuO/TC and 08CuO/ CeO_2 catalysts are obviously larger than the corresponding theoretical H_2 consumptions, implying the existence of strong interaction between copper oxide species and the supports (TC and CeO_2), which leads to the reduction of TC and CeO_2 supports.

3.3. Surface chemical states analysis (XPS)

XPS was employed to characterize the elementary oxidation states and surface compositions of these synthesized samples, and the corresponding results are displayed in Fig. 7. As shown in Fig. 7a, anatase TiO_2 exhibits two binding energy peaks of $\text{Ti } 2p_{1/2}$ and $\text{Ti } 2p_{3/2}$ at 464.1 and 458.4 eV, respectively, which are the characteristics of Ti^{4+} species [8,40]. For TC support, the binding energies of

$\text{Ti } 2p_{1/2}$ and $\text{Ti } 2p_{3/2}$ shift to low binding energy direction slightly, indicating that there are some electron interactions between Ce^{4+} and Ti^{4+} . With regard to 08CuO/ TiO_2 catalyst, its binding energies of $\text{Ti } 2p_{1/2}$ and $\text{Ti } 2p_{3/2}$ are similar with anatase TiO_2 , implying that the interaction between copper oxide species and anatase TiO_2 support is very weak, which is consistent with the results of LRS and H_2 -TPR. However, the binding energies of $\text{Ti } 2p_{1/2}$ and $\text{Ti } 2p_{3/2}$ in 08CuO/TC catalyst locate at 463.9 and 458.2 eV, respectively, which are slightly lower than those in TC support. The obtained results indicate that the incorporation of Ce^{4+} into the lattice of anatase TiO_2 may enhance the electron interaction between Cu^{2+} and Ti^{4+} , i.e., the redox cycle of $\text{Cu}^{2+} + \text{Ce}^{3+} \leftrightarrow \text{Cu}^+ + \text{Ce}^{4+}$ may promote the establishment of the other redox cycle of $\text{Cu}^{2+} + \text{Ti}^{3+} \leftrightarrow \text{Cu}^+ + \text{Ti}^{4+}$ in 08CuO/TC catalyst, which is in agreement with the literature [22].

The XPS spectrum of $\text{Ce } 3d$ is numerically fitted with eight components for each sample, and the corresponding assignments are defined in Fig. 7b. The two groups of spin-orbital multiplets attributing to $3d_{3/2}$ and $3d_{5/2}$ are denoted as u and v , which are extending in the binding energy range of 880–920 eV. It is widely reported that the bands labeled as u''' and v''' , u'' and v'' , u and v are assigned to Ce^{4+} , while the bands of u' and v' are related to Ce^{3+} [8,41]. As a result, the chemical valence state of cerium on the surface of these cerium-containing samples is mainly +4, and a part of Ce^{3+} co-exists. In addition, the percent content of Ce^{3+} in these samples can be determined by calculating the area ratio of these binding energy bands based on the following equation [41]:

$$\text{Ce}^{3+}(\%) = \frac{S_{u'} + S_{v'}}{\sum (S_u + S_v)} \times 100$$

The calculated percent content of Ce^{3+} for these cerium-containing samples is summarized in Table 3. We can find that the percent content of Ce^{3+} for CeO_2 is 14.83%, which is in accordance with the value (15%) reported in the literature [41]. For TC support, the percent content of Ce^{3+} increases to 19.69% with the incorporation of Ce^{4+} into the lattice of anatase TiO_2 , implying that there is some electron interaction between Ce^{4+} and Ti^{4+} . With regard to 08CuO/ CeO_2 catalyst, its Ce^{3+} percent content is 16.73%, which is larger than that of CeO_2 due to

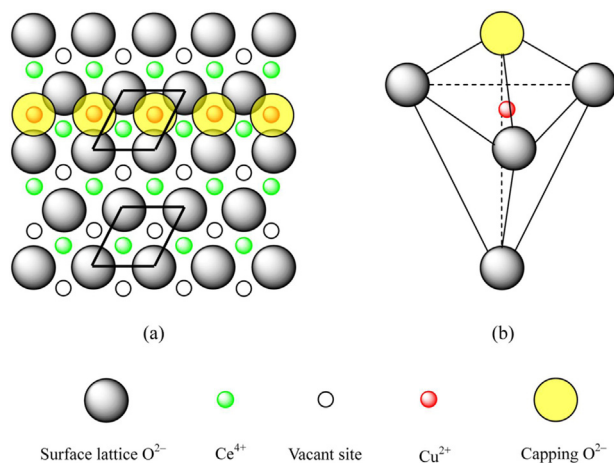


Fig. 6. The schematic diagram of (a) the dispersion of Cu^{2+} on the (111) crystal plane of CeO_2 , and (b) the corresponding coordination status of Cu^{2+} on the (111) crystal plane of CeO_2 .

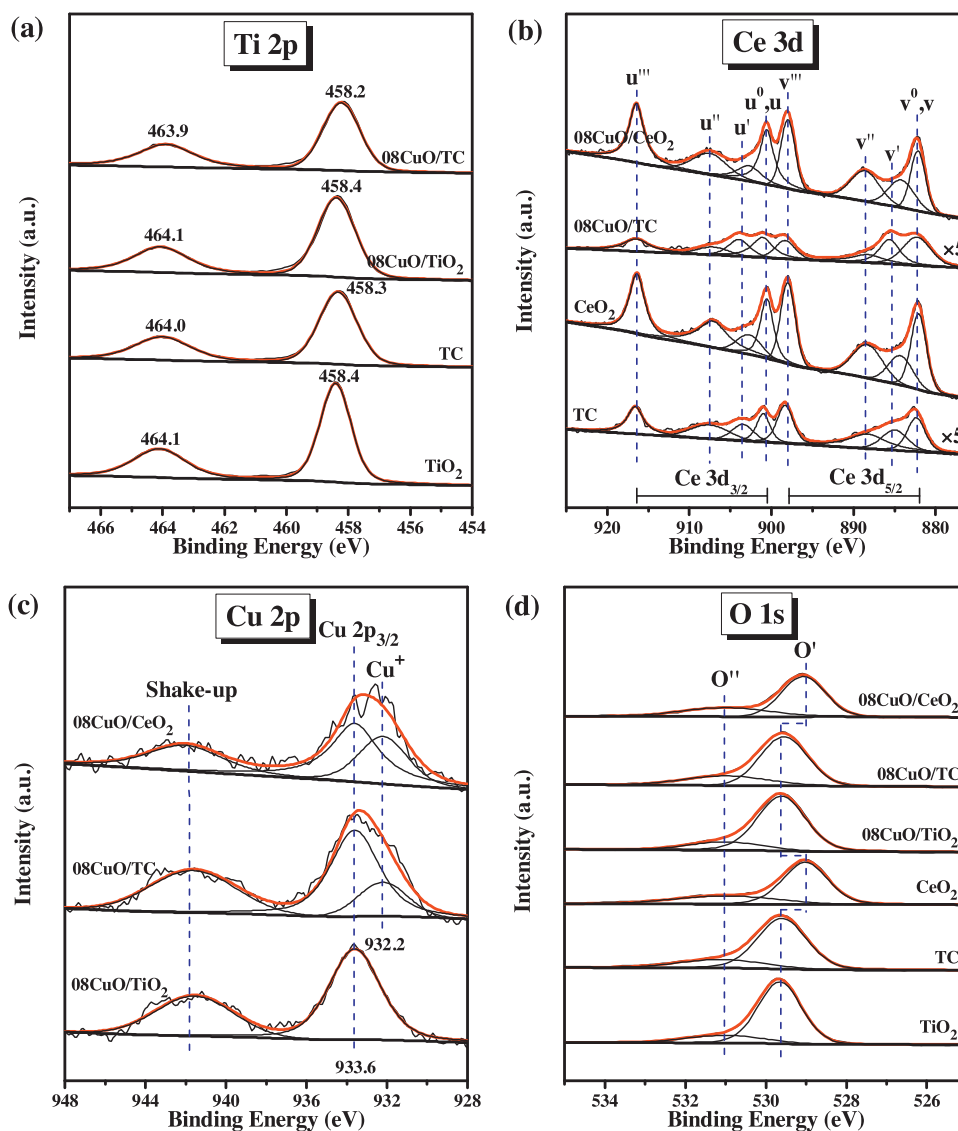


Fig. 7. XPS spectra of the obtained samples: (a) Ti 2p, (b) Ce 3d, (c) Cu 2p, and (d) O1s.

the establishment of the redox cycle ($\text{Cu}^{2+} + \text{Ce}^{3+} \leftrightarrow \text{Cu}^+ + \text{Ce}^{4+}$). Interestingly, 08CuO/TC catalyst exhibits the largest Ce^{3+} percent content (26.02%), which suggests that the synergistic effect of the redox cycles of $\text{Cu}^{2+} + \text{Ce}^{3+} \leftrightarrow \text{Cu}^+ + \text{Ce}^{4+}$ and $\text{Cu}^{2+} + \text{Ti}^{3+} \leftrightarrow \text{Cu}^+ + \text{Ti}^{4+}$ is beneficial to the generation of Ce^{3+} .

Fig. 7c shows the XPS spectrum of Cu 2p for these copper-based catalysts. It can be noticed that all these catalysts exhibit a main peak of Cu $2p_{3/2}$ at 933.6 eV and a shake-up peak exhibited in the binding energy range of 938–946 eV, which are the characteristics of Cu^{2+} species [18,38]. Furthermore, a weak peak can be detected at 932.2 eV in 08CuO/TC and 08CuO/CeO₂ catalysts, indicating

the existence of Cu^+ species [19,33]. The percent content of Cu^+ can be determined by calculating the area ratio between Cu^+ and $\text{Cu}^+ + \text{Cu}^{2+}$, and listed in Table 3. The appearance of Cu^+ species is mainly owing to the redox cycles of $\text{Cu}^{2+} + \text{Ce}^{3+} \leftrightarrow \text{Cu}^+ + \text{Ce}^{4+}$ and $\text{Cu}^{2+} + \text{Ti}^{3+} \leftrightarrow \text{Cu}^+ + \text{Ti}^{4+}$ shifting to right. However, Cu^+ species is absent in 08CuO/TiO₂ catalyst, which suggests that the electron interaction between CuO and anatase TiO₂ is very weak.

The XPS spectrum for the O 1s ionization features of these samples is numerically fitted with two components, which is presented in Fig. 7d. All the samples exhibit a primary band O' at 529.1–529.7 eV attributed to the lattice oxygen bonding to the

Table 3

The surface compositions of the obtained samples.

Samples	Atomic concentration				Atomic ratio			
	Cu (at.%)	Ti (at.%)	Ce (at.%)	O (at.%)	$\text{Cu}^+ / (\text{Cu}^+ + \text{Cu}^{2+})$ (%)	$\text{Ce}^{3+} / (\text{Ce}^{3+} + \text{Ce}^{4+})$ (%)	O'/(Cu + Ti + Ce)	O''/(O' + O'') (%)
TiO ₂	–	21.74	–	57.18	–	–	2.63 (2.00)	17.54
TC	–	18.91	1.69	56.68	–	19.69	2.75 (2.00)	21.37
CeO ₂	–	–	17.75	50.51	–	14.83	2.85 (2.00)	28.88
08CuO/TiO ₂	4.34	19.90	–	55.45	0	–	2.29 (1.96)	17.64
08CuO/TC	4.49	18.17	1.32	54.49	23.79	26.02	2.27 (1.93)	25.83
08CuO/CeO ₂	4.21	–	17.11	49.34	38.40	16.73	2.31 (1.94)	31.25

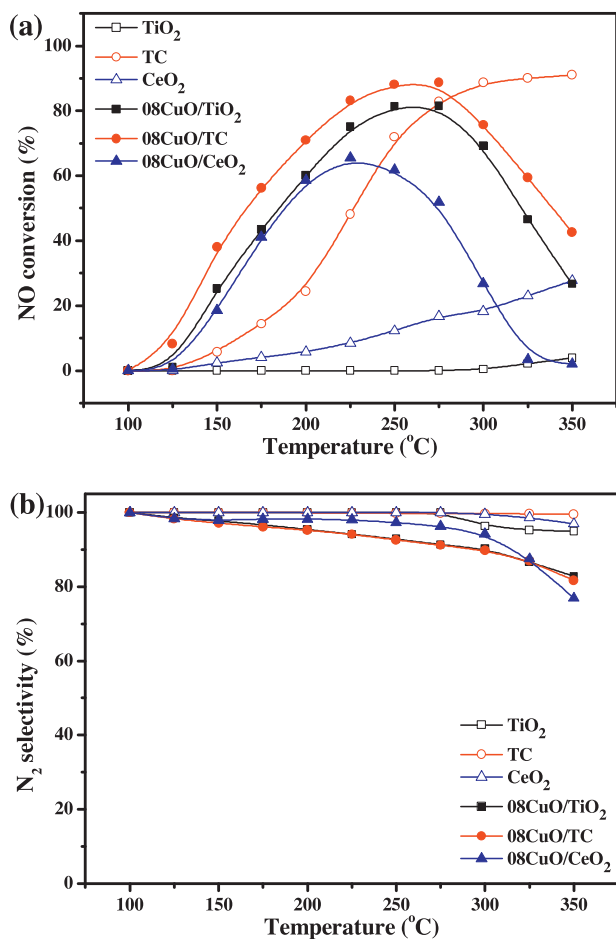


Fig. 8. Catalytic performances of these synthesized samples for NO + NH₃ + O₂ model reaction: (a) NO conversion, and (b) N₂ selectivity.

metal cations, and a shoulder band O'' at higher binding energy (531.0 eV) assigned to the chemisorbed oxygen or/and the oxygen species of surface hydroxyl and adsorbed water [8,42]. It can be seen from Table 3 that the atomic ratio of O/(Cu + Ti + Ce) for each sample is higher than its corresponding nominal value in the full oxidation state, indicating the adsorption of the chemisorbed oxygen or/and the oxygen species of surface hydroxyl and adsorbed water on the surface of the samples. Moreover, the proportion of O''/(O' + O'') for these samples increases with the incorporation of Ce⁴⁺ and the loading of CuO (except for 08CuO/TiO₂ catalyst). The possible reason is that the incorporation of Ce⁴⁺ and the loading of CuO result in the generation of low-valence state metal cations, which can create the charge imbalance, oxygen vacancy, and unsaturated chemical bond on the surface of these samples, and further adsorb the chemisorbed oxygen or/and the weakly bonded oxygen species [8].

3.4. Catalytic performance measurements (NO + NH₃ + O₂ model reaction)

The catalytic performances of these synthesized samples for NH₃-SCR of NO in the presence of excess oxygen are given in Fig. 8. In the whole operation temperature range (100–350 °C), we can see from Fig. 8a that the activities of anatase TiO₂ and CeO₂ supports are very poor (lower than 30%), and increase slowly with the elevation of temperature. For TC support, its activity is obviously better than anatase TiO₂ and CeO₂ supports due to the electron interaction between Ti⁴⁺ and Ce⁴⁺, and it shows the optimal

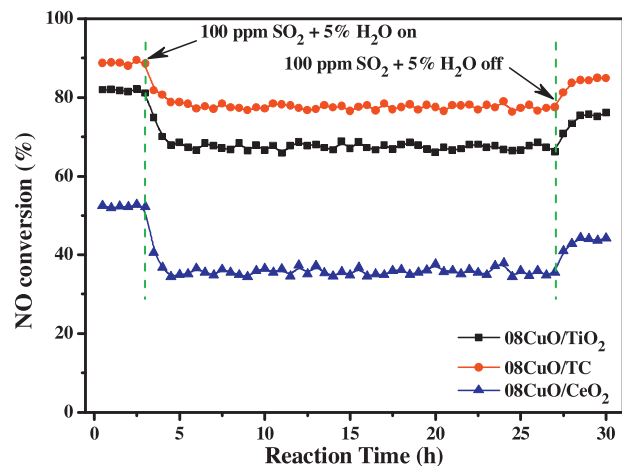


Fig. 9. The H₂O and SO₂ durability of these copper-based catalysts at 275 °C.

activity in the temperature range of 300–350 °C, which is consistent with the literatures [8,22]. However, the low-temperature (below 300 °C) activity of TC support is still unsatisfactory. With regard to 08CuO/TiO₂, 08CuO/TC, and 08CuO/CeO₂ catalysts, the low-temperature (below 300 °C) activities are enhanced remarkably compared with each corresponding support, which indicates that copper oxide species is the mainly active component in the low temperature range (100–275 °C). Furthermore, the activities of these copper-based catalysts exhibit a similar variation trend, which increase up to a maximum value with the elevation of temperature firstly, and then decrease with the further increase of temperature. The elevation of temperature can provide more energy to promote the proceeding of NO reduction by NH₃, so the activities are enhanced greatly in the low temperature range. While the oxidation of NH₃, which consumes the amount of reductant NH₃ and generates reactant NO, becomes dominating reaction at higher temperatures and consequently results in the decrease of activities. Interestingly, we can observe that the activities of these copper-based catalysts are ranked by 08CuO/CeO₂ < 08CuO/TiO₂ < 08CuO/TC in the whole operation temperature range (100–350 °C), which suggests that the incorporation of Ce⁴⁺ into the lattice of anatase TiO₂ can enhance the activity of 08CuO/TiO₂ catalyst obviously. Fig. 8b displays that N₂ selectivities of these synthesized samples show a similar variation trend, which decrease slightly with the elevation of temperature owing to the formation of N₂O and NO₂ at higher temperatures. Simultaneously, we can find that the incorporation of Ce⁴⁺ into the lattice of anatase TiO₂ has almost no influence on the N₂ selectivity of 08CuO/TiO₂ catalyst.

The water and sulfur resistance performances of these copper-based catalysts at 275 °C are also evaluated in the present work, and the corresponding results are presented in Fig. 9. It can be noticed from Fig. 9 that when H₂O and SO₂ are introduced into the catalytic reaction system, the activities of these copper-based catalysts decrease firstly, wherein the loss of activities is attributed to the deposition of ammonium sulfate on the surface of the catalysts [3], and then the activities keep stable, which is similar with the results of Liu et al. [22]. Once H₂O and SO₂ are shut down, the activities of these copper-based catalysts recover to some extent, but are slightly lower than the initial activities. Furthermore, we can find that the decrease of the activity for 08CuO/TC catalyst is the slightest among these copper-based catalysts, which indicates that the incorporation of Ce⁴⁺ into the lattice of anatase TiO₂ can enhance the water and sulfur resistance performance of 08CuO/TiO₂ catalyst efficiently.

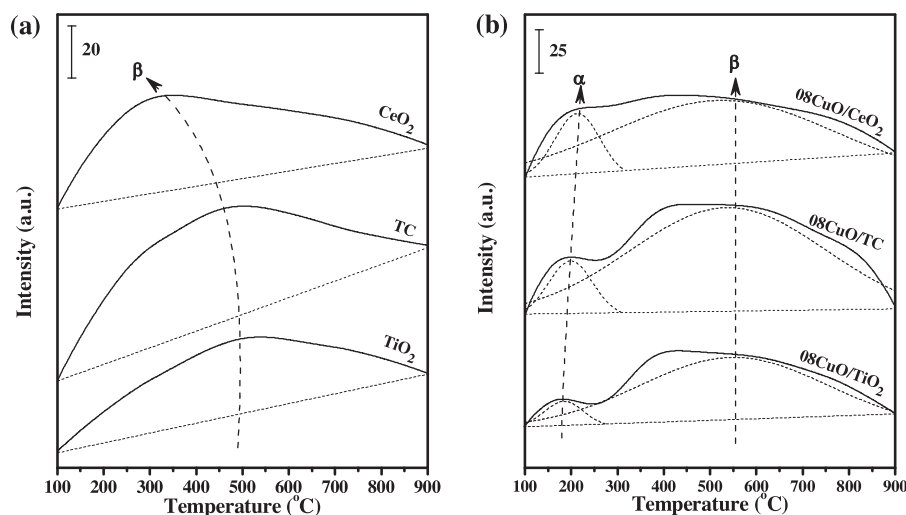


Fig. 10. NH_3 -TPD profiles of the obtained samples: (a) supports, and (b) catalysts.

3.5. Surface acidities (NH_3 -TPD and NH_3 adsorption *in situ* DRIFTS)

It is well known that the surface acidities of the catalysts play an important role in the catalytic performance for NH_3 -SCR of NO in the presence of excess oxygen. As a result, NH_3 -TPD experiments are carried out, as shown in Fig. 10. The NH_3 -TPD profiles of anatase TiO_2 , TC, and CeO_2 supports exhibit a broad peak at higher temperature (labeled as β) attributed to strong acid site (Fig. 10a). The quantitative analysis results of NH_3 -TPD are summarized in Table 4, we can find that the desorption peak area follows the sequence of anatase $\text{TiO}_2 < \text{CeO}_2 < \text{TC}$, which suggests that the incorporation of Ce^{4+} into the lattice of anatase TiO_2 can increase its amount of strong acid site obviously. Fig. 10b shows that when copper oxide species are loaded on the surface of these supports, two desorption peaks can be observed for these copper-based catalysts, indicating that there are two kinds of acid sites on the surface of the catalysts. The first peak at lower temperature (labeled as α) is assigned to weak acid site, and the other at higher temperature (labeled as β) is related to strong acid site. Table 4 displays that both the amounts of weak acid site and strong acid site of 08CuO/TC catalyst are larger than those of 08CuO/ TiO_2 catalyst due to the unstable distorted octahedral coordination structure of Cu^{2+} in 08CuO/TC catalyst and the synergistic effect of the dual redox cycles ($\text{Cu}^{2+} + \text{Ce}^{3+} \leftrightarrow \text{Cu}^+ + \text{Ce}^{4+}$ and $\text{Cu}^{2+} + \text{Ti}^{3+} \leftrightarrow \text{Cu}^+ + \text{Ti}^{4+}$).

The reaction mechanism of selective catalytic reduction of NO by NH_3 in the presence of excess oxygen ($\text{NO} + \text{NH}_3 + \text{O}_2$ model reaction) has been investigated extensively, and the surface acidity is considered to be closely related to the catalytic activity [12,14,43]. However, whether the Brønsted acid site or Lewis acid site is the active site for this model reaction is still controversial. Moreover, NH_3 -TPD can determine the total amount of acid site,

Table 4
The quantitative analysis data of NH_3 -TPD over the obtained samples.

Samples	Weak acid (S_α) (a.u.)	Strong acid (S_β) (a.u.)	Total acid ($S_\alpha + S_\beta$) (a.u.)
TiO_2	–	13,807	13,807
TC	–	21,083	21,083
CeO_2	–	17,175	17,175
08CuO/ TiO_2	1219	15,199	16,418
08CuO/TC	3204	23,461	26,665
08CuO/ CeO_2	3844	16,254	20,098

but still cannot distinguish the Brønsted acid site and Lewis acid site. Therefore, NH_3 adsorption *in situ* DRIFTS is employed to solve this problem, and the corresponding results are exhibited in Fig. 11. For 08CuO/ TiO_2 catalyst (Fig. 11a), when exposing it to NH_3 - N_2 (1% of NH_3 by volume) for 1 h and purged by high purified N_2 for 1 h at 25 °C, several bands are detected in the range of 1100–1700 cm^{-1} . According to the literatures, the bands at 1615 and 1224 cm^{-1} are attributed to the asymmetric and symmetric bending vibrations of N–H bond in NH_3 coordinately linked to Lewis acid site [44–46]. When the temperature increases to 75 °C, a new band appears at 1150 cm^{-1} , which is also assigned to the symmetric bending vibration of N–H bond in NH_3 coordinately linked to Lewis acid site [44]. These adsorbed NH_3 species desorb with the further increase of temperature, and disappear completely at 375 °C. The obtained results suggest that there is only Lewis acid site on the surface of 08CuO/ TiO_2 catalyst without Brønsted acid site. Fig. 11b shows the results of NH_3 adsorption on the surface of 08CuO/TC catalyst, similarly, only the asymmetric and symmetric bending vibrations of N–H bond in NH_3 coordinately linked to Lewis acid site can be observed at 1613 cm^{-1} and 1218, 1153 cm^{-1} . Compared with 08CuO/ TiO_2 catalyst, the band for the symmetric bending vibration of N–H bond in NH_3 coordinately linked to Lewis acid site (1153 cm^{-1}) appears at lower temperature of 25 °C, the possible reason is that the distorted octahedral coordination structure of Cu^{2+} in 08CuO/TC catalyst is more unstable than the stable octahedral coordination structure of Cu^{2+} in 08CuO/ TiO_2 catalyst, which leads to the exacerbation of vibration of N–H bond. Finally, all these vibration bands of N–H bond related to Lewis acid site also disappear completely at 375 °C due to thermal desorption. With regard to 08CuO/ CeO_2 catalyst (Fig. 11c), the bands for the asymmetric and symmetric bending vibrations of N–H bond in NH_3 coordinately linked to Lewis acid site can be detected at 1632 and 1221 cm^{-1} , respectively, while the band for the asymmetric bending vibration of N–H bond in NH_4^+ chemisorbed on Brønsted acid site can be observed at 1435 cm^{-1} [12,44]. With the temperature increases to 100 °C, several new bands appear at 1548, 1505, and 1356 cm^{-1} , the first band is attributed to the asymmetric bending vibration of N–H bond in $-\text{NH}_3^+$ group, which generates from the decomposition of NH_4^+ chemisorbed on Brønsted acid site, and the last two bands are related to scissoring and wagging vibrations of $-\text{NH}_2$ species, which is formed by hydrogen abstraction from NH_3 coordinately linked to Lewis acid site [12,44]. These vibration bands increase with the further elevation of temperature firstly, and then decrease

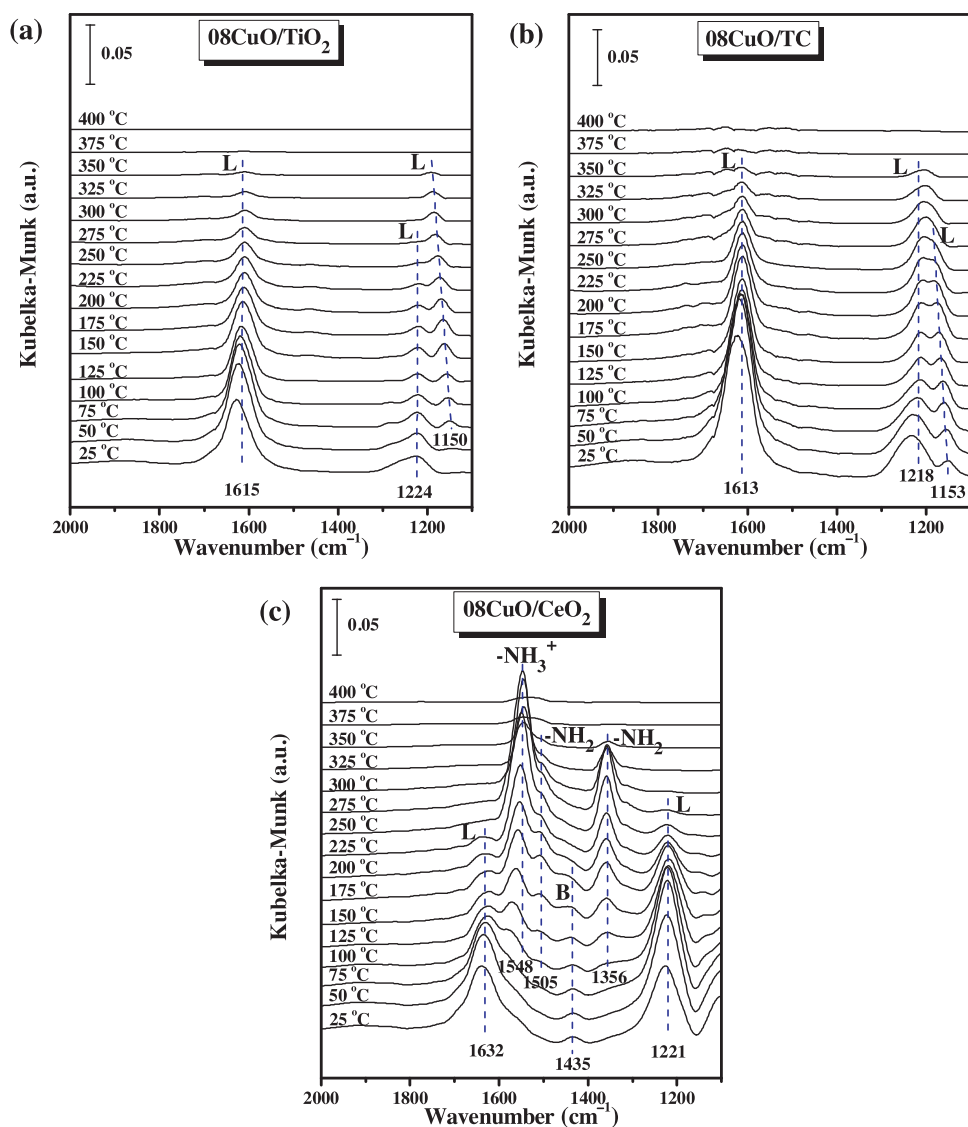


Fig. 11. NH_3 adsorption *in situ* DRIFTS of these copper-based catalysts: (a) 08CuO/ TiO_2 , (b) 08CuO/TC, and (c) 08CuO/ CeO_2 .

and disappear. Simultaneously, we can find that all the adsorbed NH_3 species on Brønsted acid site and Lewis acid site disappear completely at 300 °C owing to decomposition and desorption.

Combining the catalytic performances and NH_3 adsorption *in situ* DRIFTS results, we can find that 08CuO/TC catalyst only possesses Lewis acid site without Brønsted acid site, but it exhibits the best catalytic performance, which indicates that Lewis acid site is more active than Brønsted acid site in our present work. As a result, the variation trend of the integrated intensity of the bands related to Lewis acid site has been investigated as a function of temperature, as shown in Fig. 12. From this figure, we can notice that the amount of Lewis acid site follows the order (25 °C): 08CuO/ TiO_2 < 08CuO/ CeO_2 < 08CuO/TC, which indicates that the incorporation of Ce^{4+} into the lattice of anatase TiO_2 can create more Lewis acid sites on the surface of 08CuO/TC catalyst owing to the unstable distorted octahedral coordination structure of Cu^{2+} in 08CuO/TC catalyst and the synergistic effect of the dual redox cycles ($\text{Cu}^{2+} + \text{Ce}^{3+} \leftrightarrow \text{Cu}^+ + \text{Ce}^{4+}$ and $\text{Cu}^{2+} + \text{Ti}^{3+} \leftrightarrow \text{Cu}^+ + \text{Ti}^{4+}$). While the decomposition and desorption of the adsorbed NH_3 species on the surface of 08CuO/ CeO_2 catalyst are the easiest due to the excellent oxygen storage capacity of CeO_2 , which is beneficial to the oxidation of NH_3 and the selective catalytic reduction of NO by NH_3 .

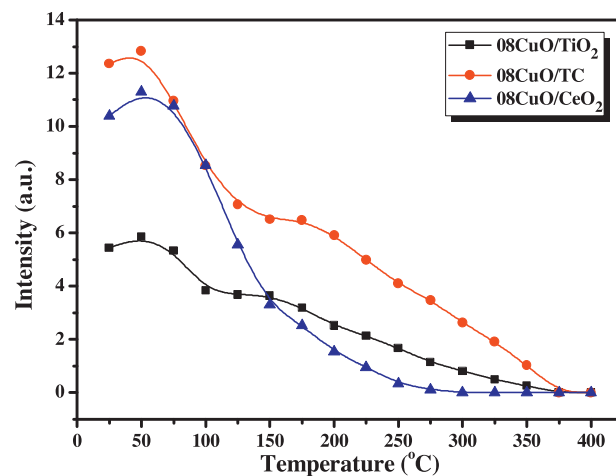


Fig. 12. Integrated intensity of the bands in NH_3 adsorption *in situ* DRIFTS related to Lewis acid site over these copper-based catalysts as a function of temperature.

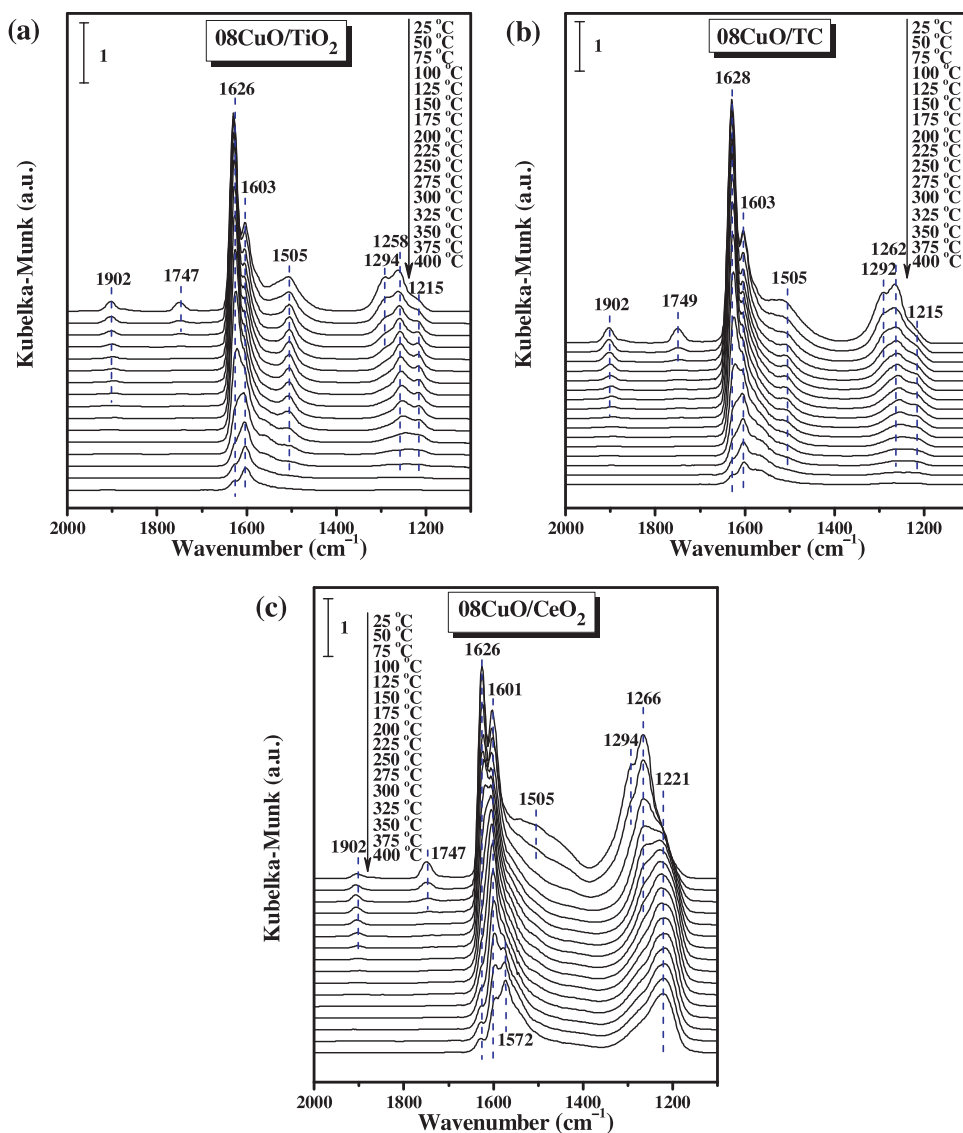


Fig. 13. NO + O₂ adsorption *in situ* DRIFTS of these copper-based catalysts: (a) 08CuO/TiO₂, (b) 08CuO/TC, and (c) 08CuO/CeO₂.

3.6. Adsorption behaviors (NO + O₂ adsorption *in situ* DRIFTS)

The results of NH₃ adsorption *in situ* DRIFTS and catalytic performance measurements indicate that 08CuO/CeO₂ catalyst exhibits the best ability to activate NH₃, but its catalytic performance for the selective catalytic reduction of NO by NH₃ is the worst among these copper-based catalysts in the present work. In order to clarify the reason, NO + O₂ adsorption *in situ* DRIFTS of these copper-based catalysts are recorded in Fig. 13. For 08CuO/TiO₂ catalyst (Fig. 13a), when NO + O₂ mixed gases are introduced into the DRIFTS cell at room temperature, several vibration bands can be detected in the range of 1000–2000 cm⁻¹, the gaseous NO molecules exhibit a weak band at 1902 cm⁻¹; the physisorbed NO species appear at 1747 cm⁻¹; the bridging bidentate nitrates give a N=O stretching vibration band at 1626 cm⁻¹; the bridging monodentate nitrates display a shoulder band at 1603 cm⁻¹; the monodentate nitrates show two bands at 1505 and 1294 cm⁻¹; the linear nitrites present a vibration mode at 1258 cm⁻¹; furthermore, the chelating bidentate nitrates give a band at 1215 cm⁻¹ [33,44,47,48]. With the increase of temperature to 75 °C, the physisorbed NO species disappear due to the thermal desorption. Further heating to 375 °C results in the disappearance of monodentate nitrates,

linear nitrites, and chelating bidentate nitrates, indicating that these adsorbed NO species on the surface of 08CuO/TiO₂ catalyst can be desorbed/decomposed/transformed during the heating process. Moreover, we can find that the band intensities of bridging bidentate nitrates and bridging monodentate nitrates weaken with the elevation of temperature obviously, but not disappear even at 400 °C. With regard to 08CuO/TC catalyst (Fig. 13b), similarly, all the bands for gaseous NO molecules, physisorbed NO species, bridging bidentate nitrates, bridging monodentate nitrates, monodentate nitrates, linear nitrites, and chelating bidentate nitrates also appear at the corresponding positions at 25 °C. And the variation trend of these bands of 08CuO/TC catalyst is very similar with those of 08CuO/TiO₂ catalyst. Interestingly, we can find that the band intensities of these adsorbed NO species on the surface of 08CuO/TC catalyst are stronger than those on the surface of 08CuO/TiO₂ catalyst, indicating that the incorporation of Ce⁴⁺ into the lattice of anatase TiO₂ can improve the adsorption amount of NO species on the surface of 08CuO/TiO₂ catalyst efficiently, which is beneficial to the enhancement of catalytic performance for the selective catalytic reduction of NO by NH₃. Fig. 13c shows that all the adsorbed NO species can be observed on the surface of 08CuO/CeO₂ catalyst at 25 °C. And there are some obvious differences with 08CuO/TiO₂

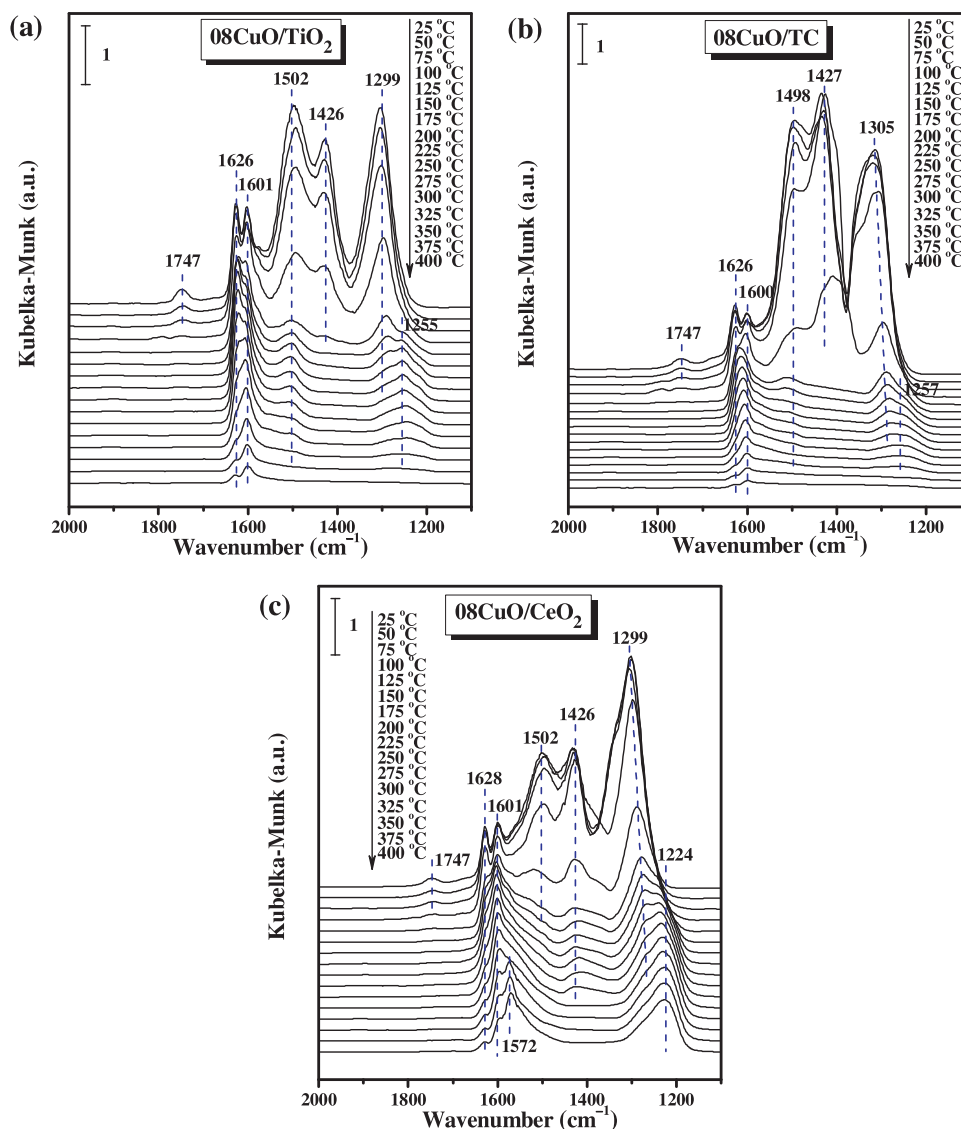


Fig. 14. NO + O₂ adsorption *in situ* DRIFTS of these copper-based catalysts pre-adsorbed NH₃: (a) 08CuO/TiO₂, (b) 08CuO/TC, and (c) 08CuO/CeO₂.

and 08CuO/TC catalysts during the heating process: firstly, with the increase of temperature to 350 °C, the chelating bidentate nitrates present another vibration band at 1572 cm⁻¹ [33,47]; secondly, the two bands for chelating bidentate nitrates (1572 and 1221 cm⁻¹) keep stable with further elevation of temperature even at 400 °C; finally, the band intensities of bridging bidentate nitrates and bridging monodentate nitrates (1626 and 1601 cm⁻¹, respectively) on the surface of 08CuO/CeO₂ catalyst are obviously stronger than those on the surface of 08CuO/TiO₂ and 08CuO/TC catalysts at higher temperature. These phenomena suggest that the desorption/decomposition/transformation of these adsorbed NO species on the surface of 08CuO/CeO₂ catalyst is more difficult than those on the surface of 08CuO/TiO₂ and 08CuO/TC catalysts, which is not conducive to the proceeding of the selective catalytic reduction of NO by NH₃. Combining with the results of NH₃ adsorption *in situ* DRIFTS, we can find that 08CuO/CeO₂ catalyst can promote the decomposition and desorption of NH₃ due to the excellent oxygen storage capacity of CeO₂, but is not beneficial to the desorption/decomposition/transformation of the adsorbed NO species. Therefore, 08CuO/CeO₂ catalyst is conducive to the occurrence of the side reaction of NH₃ oxidation rather than NO reduction by

NH₃, which leads to the poor catalytic performance for the selective catalytic reduction of NO by NH₃.

In order to further explore the reason for the difference of the catalytic performance for NH₃-SCR of NO in the presence of excess oxygen on the surface of these copper-based catalysts in the present work, *in situ* DRIFTS technique is employed to investigate the reaction between NO + O₂ and pre-adsorbed NH₃ species over these copper-based catalysts, and the corresponding results are displayed in Fig. 14. After NH₃ pre-adsorption and high purified N₂ purging at 25 °C, the catalysts are saturated by NO + O₂. For 08CuO/TiO₂ catalyst (Fig. 14a), several kinds of nitrates and physisorbed NO species can be detected at the corresponding positions, which is similar with the above-mentioned NO + O₂ adsorption *in situ* DRIFTS results. However, compared with Fig. 13a, the bands for monodentate nitrates (1502 and 1299 cm⁻¹) become stronger, which is probably due to the formation of NH₄NO₃ species. In addition, a new band appears at 1426 cm⁻¹, which is attributed to NH₄NO₂ species [5,49]. According to the NH₃ adsorption *in situ* DRIFTS results, there is only Lewis acid site on the surface of 08CuO/TiO₂ catalyst without Brønsted acid site. Therefore, the formation of NH₄NO₃ and NH₄NO₂ species probably

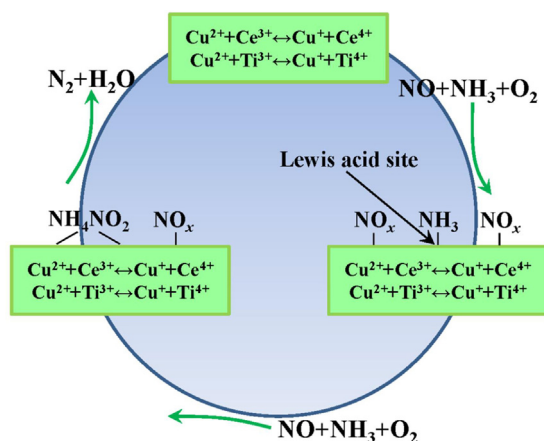


Fig. 15. Possible reaction mechanism (schematic diagram) of NH_3 -SCR of NO in the presence of excess oxygen over 08CuO/TC catalyst.

results from the complex electron interaction between NH_3 coordinated on Lewis acid site and surface adsorbed NO species. With the increase of temperature to 150°C , the band at 1426 cm^{-1} disappears completely, and the bands at 1502 and 1299 cm^{-1} weaken obviously, which is owing to the decomposition of NH_4NO_2 and NH_4NO_3 species. When the temperature is higher than 150°C , the variation trend of the adsorbed NO species is the same as the above-mentioned $\text{NO} + \text{O}_2$ adsorption *in situ* DRIFTS in Fig. 13a. With regard to 08CuO/TC catalyst (Fig. 14b), the results of $\text{NO} + \text{O}_2$ adsorption *in situ* DRIFTS of 08CuO/TC catalyst pre-adsorbed NH_3 are very similar with those of 08CuO/ TiO_2 catalyst pre-adsorbed NH_3 . According to the literature, NH_4NO_2 species is an important intermediate product in NH_3 -SCR of NO process, which can decompose into the final products of N_2 and H_2O , and promote the enhancement of catalytic performance for NH_3 -SCR of NO in the presence of excess oxygen [49]. Interestingly, we can notice that the intensity of the band for NH_4NO_2 species (1427 cm^{-1}) on the surface of 08CuO/TC catalyst is obviously stronger than that on the surface of 08CuO/ TiO_2 catalyst, indicating that the catalytic performance of 08CuO/TC catalyst is better than that of 08CuO/ TiO_2 catalyst for NH_3 -SCR of NO in the presence of excess oxygen, which is consistent with the catalytic performance measurements. In view of 08CuO/ CeO_2 catalyst (Fig. 14c), it is noteworthy that the intensity of the band for NH_4NO_2 species (1426 cm^{-1}) on the surface of 08CuO/ CeO_2 catalyst is obviously weaker than that on the surface of 08CuO/ TiO_2 and 08CuO/TC catalysts, and difficult to disappear due to the adsorption of NH_4^+ on Brønsted acid site of 08CuO/ CeO_2 catalyst, which indicate that the catalytic performance of 08CuO/ CeO_2 catalyst for NH_3 -SCR of NO in the presence of excess oxygen is the worst among these copper-based catalysts in the present work.

3.7. Possible reaction mechanism of $\text{NO} + \text{NH}_3 + \text{O}_2$ model reaction

Based on the above-mentioned characterizations, a possible reaction mechanism (schematic diagram) of NH_3 -SCR of NO in the presence of excess oxygen over 08CuO/TC catalyst under the current conditions is tentatively proposed in Fig. 15. The unstable distorted octahedral coordination structure of Cu^{2+} in 08CuO/TC catalyst and the synergistic effect of the dual redox cycles ($\text{Cu}^{2+} + \text{Ce}^{3+} \leftrightarrow \text{Cu}^+ + \text{Ce}^{4+}$ and $\text{Cu}^{2+} + \text{Ti}^{3+} \leftrightarrow \text{Cu}^+ + \text{Ti}^{4+}$) may promote the formation of more Lewis acid sites on the surface of 08CuO/TC catalyst, which is supported by NH_3 adsorption *in situ* DRIFTS. Therefore, when the reactant gases of $\text{NO} + \text{NH}_3 + \text{O}_2$ are introduced into the catalytic reaction system, NH_3 will coordinately adsorb on the Lewis acid site of 08CuO/TC catalyst. And then, because of the complex electron interaction between reactant molecules (NO ,

NH_3 , and O_2) and 08CuO/TC catalyst, the intermediate product of NH_4NO_2 species can be generated on the surface of 08CuO/TC catalyst. With the elevation of temperature, NH_4NO_2 species further decomposes into the final products of N_2 and H_2O . In summary, the incorporation of Ce^{4+} into the lattice of anatase TiO_2 may enhance the electron interaction between copper oxide species and TC support through the redox cycles of $\text{Cu}^{2+} + \text{Ce}^{3+} \leftrightarrow \text{Cu}^+ + \text{Ce}^{4+}$ and $\text{Cu}^{2+} + \text{Ti}^{3+} \leftrightarrow \text{Cu}^+ + \text{Ti}^{4+}$, which is beneficial to the formation of more Lewis acid sites and the activation of the reactant molecules to generate more NH_4NO_2 species, and further promote the enhancement of catalytic performance for NH_3 -SCR of NO in the presence of excess oxygen.

4. Conclusions

In the present work, $\text{Ti}_{0.95}\text{Ce}_{0.05}\text{O}_2$ (TC) solid solution was synthesized by incorporating Ce^{4+} into the lattice of anatase TiO_2 , and then used as a support to prepare $\text{CuO}/\text{Ti}_{0.95}\text{Ce}_{0.05}\text{O}_2$ (CuO/TC) catalyst. Furthermore, CuO/TiO_2 and CuO/CeO_2 catalysts were also prepared for comparison. Especially, the structure, dispersion, reduction, surface composition, acidity, adsorption, and catalytic performance of these synthesized catalysts for NH_3 -SCR of NO in the presence of excess oxygen have been investigated systematically. Combining with the above-mentioned characterization results, several conclusions can be drawn as follows:

- (1) The incorporation of Ce^{4+} into the lattice of anatase TiO_2 to form TC solid solution may inhibit the grain growth of anatase TiO_2 , which leads to the decrease of crystallite size and the enlargement of BET specific surface area.
- (2) Lewis acid site on the surface of these copper-based catalysts plays an important role in $\text{NO} + \text{NH}_3 + \text{O}_2$ model reaction.
- (3) The unstable distorted octahedral coordination structure of Cu^{2+} in 08CuO/TC catalyst and the synergistic effect of the dual redox cycles ($\text{Cu}^{2+} + \text{Ce}^{3+} \leftrightarrow \text{Cu}^+ + \text{Ce}^{4+}$ and $\text{Cu}^{2+} + \text{Ti}^{3+} \leftrightarrow \text{Cu}^+ + \text{Ti}^{4+}$) may promote the formation of more Lewis acid sites on the surface of 08CuO/TC catalyst and the activation of reactant molecules to generate more NH_4NO_2 species, which are conducive to the enhancement of catalytic performance for NH_3 -SCR of NO in the presence of excess oxygen.

Acknowledgements

The financial supports of the National Natural Science Foundation of China (Nos. 20973091, 21273110), the National Basic Research Program of China (973 program, Nos. 2009CB623500, 2010CB732300), Jiangsu Province Science and Technology Support Program (Industrial, BE2011167), and Jiangsu Province Scientific Research Foundation for Graduate (No. CXZZ12.0038) are gratefully acknowledged.

Appendix A. Supplementary data

Supplementary data associated with this article can be found, in the online version, at <http://dx.doi.org/10.1016/j.apcatb.2013.12.007>.

References

- [1] Y.S. Shen, Y.F. Ma, S.M. Zhu, Catal. Sci. Technol. 2 (2012) 589–599.
- [2] X.J. Yao, C.J. Tang, Z.Y. Ji, Y. Dai, Y. Cao, F. Gao, L. Dong, Y. Chen, Catal. Sci. Technol. 3 (2013) 688–698.
- [3] Y. Peng, C.X. Liu, X.Y. Zhang, J.H. Li, Appl. Catal. B: Environ. 140–141 (2013) 276–282.
- [4] S. Roy, M.S. Hegde, G. Madras, Appl. Energy 86 (2009) 2283–2297.

- [5] X.Q. Wang, A.J. Shi, Y.F. Duan, J. Wang, M.Q. Shen, *Catal. Sci. Technol.* 2 (2012) 1386–1395.
- [6] A.J. Shi, X.Q. Wang, T. Yu, M.Q. Shen, *Appl. Catal. B: Environ.* 106 (2011) 359–369.
- [7] S.M. Lee, K.H. Park, S.C. Hong, *Chem. Eng. J.* 195–196 (2012) 323–331.
- [8] X. Gao, Y. Jiang, Y. Zhong, Z.Y. Luo, K.F. Cen, *J. Hazard. Mater.* 174 (2010) 734–739.
- [9] R.Y. Qu, X. Gao, K.F. Cen, J.H. Li, *Appl. Catal. B: Environ.* 142–143 (2013) 290–297.
- [10] M. Moliner, C. Franch, E. Palomares, M. Grill, A. Corma, *Chem. Commun.* 48 (2012) 8264–8266.
- [11] Y. Shu, H. Sun, X. Quan, S. Chen, *J. Phys. Chem. C* 116 (2012) 25319–25327.
- [12] J. Zhu, F. Gao, L.H. Dong, W.J. Yu, L. Qi, Z. Wang, L. Dong, Y. Chen, *Appl. Catal. B: Environ.* 95 (2010) 144–152.
- [13] S. Tamm, S. Fogel, P. Gabrielsson, M. Skoglundh, L. Olsson, *Appl. Catal. B: Environ.* 136–137 (2013) 168–176.
- [14] T. Boningari, R. Koirala, P.G. Smirniotis, *Appl. Catal. B: Environ.* 127 (2012) 255–264.
- [15] C.X. Liu, L. Chen, J.H. Li, L. Ma, H. Arandiyán, Y. Du, J.Y. Xu, J.M. Hao, *Environ. Sci. Technol.* 46 (2012) 6182–6189.
- [16] B.M. Reddy, A. Khan, *Catal. Rev.* 47 (2005) 257–296.
- [17] C.Z. Sun, L.H. Dong, W.J. Yu, L.C. Liu, H. Li, F. Gao, L. Dong, Y. Chen, *J. Mol. Catal. A: Chem.* 346 (2011) 29–38.
- [18] Z.C. Si, D. Weng, X.D. Wu, Y. Jiang, B. Wang, *Catal. Sci. Technol.* 1 (2011) 453–461.
- [19] Z.C. Si, D. Weng, X.D. Wu, J. Li, G. Li, *J. Catal.* 271 (2010) 43–51.
- [20] J.A. Sullivan, J.A. Doherty, *Appl. Catal. B: Environ.* 55 (2005) 185–194.
- [21] D. Pietrogiaconi, D. Sannino, A. Magliano, P. Ciambelli, S. Tuti, V. Indovina, *Appl. Catal. B: Environ.* 36 (2002) 217–230.
- [22] Z.M. Liu, Y. Yi, J.H. Li, S.I. Woo, B.Y. Wang, X.Z. Cao, Z.X. Li, *Chem. Commun.* 49 (2013) 7726–7728.
- [23] J. Zhang, W.Q. Peng, Z.H. Chen, H. Chen, L.Y. Han, *J. Phys. Chem. C* 116 (2012) 19182–19190.
- [24] Y. Chen, L.F. Zhang, *Catal. Lett.* 12 (1992) 51–62.
- [25] B. Xu, L. Dong, Y. Chen, *J. Chem. Soc., Faraday Trans.* 94 (1998) 1905–1909.
- [26] C.Z. Sun, J. Zhu, Y.Y. Lv, L. Qi, B. Liu, F. Gao, K.Q. Sun, L. Dong, Y. Chen, *Appl. Catal. B: Environ.* 103 (2011) 206–220.
- [27] H.Y. Zhu, M.M. Shen, Y. Kong, J.M. Hong, Y.H. Hu, T.D. Liu, L. Dong, Y. Chen, C. Jian, Z. Liu, *J. Mol. Catal. A: Chem.* 219 (2004) 155–164.
- [28] L. Dong, X.J. Yao, Y. Chen, *Chin. J. Catal.* 34 (2013) 851–864.
- [29] Y.V. Kolen'ko, K.A. Kovnir, A.I. Gavrilov, A.V. Garshev, P.E. Meskin, B.R. Churagulov, M. Bouchard, C. Colbeau-Justin, O.I. Lebedev, G. Van Tendeloo, M. Yoshimura, *J. Phys. Chem. B* 109 (2005) 20303–20309.
- [30] X.J. Yao, F. Gao, Q. Yu, L. Qi, C.J. Tang, L. Dong, Y. Chen, *Catal. Sci. Technol.* 3 (2013) 1355–1366.
- [31] Q.G. Dai, S.X. Bai, Z.Y. Wang, X.Y. Wang, G.Z. Lu, *Appl. Catal. B: Environ.* 126 (2012) 64–75.
- [32] J.F. Chen, Y.Y. Zhan, J.J. Zhu, C.Q. Chen, X.Y. Lin, Q. Zheng, *Appl. Catal. A: Gen.* 377 (2010) 121–127.
- [33] X.J. Yao, Q. Yu, Z.Y. Ji, Y.Y. Lv, Y. Cao, C.J. Tang, F. Gao, L. Dong, Y. Chen, *Appl. Catal. B: Environ.* 130–131 (2013) 293–304.
- [34] Z. Wang, Z.P. Qu, X. Quan, Z. Li, H. Wang, R. Fan, *Appl. Catal. B: Environ.* 134–135 (2013) 153–166.
- [35] H.L. Chen, H.Y. Zhu, Y. Wu, F. Gao, L. Dong, J.J. Zhu, *J. Mol. Catal. A: Chem.* 255 (2006) 254–259.
- [36] N.W. Hurst, S.J. Gentry, A. Jones, B.D. McNicol, *Catal. Rev.* 24 (1982) 233–309.
- [37] B. Xu, L. Dong, Y.N. Fan, Y. Chen, *J. Catal.* 193 (2000) 88–95.
- [38] L.J. Liu, Z.J. Yao, Y. Deng, F. Gao, B. Liu, L. Dong, *ChemCatChem* 3 (2011) 978–989.
- [39] L.J. Liu, J.G. Cai, L. Qi, Q. Yu, K.Q. Sun, B. Liu, F. Gao, L. Dong, Y. Chen, *J. Mol. Catal. A: Chem.* 327 (2010) 1–11.
- [40] Y.G. Wang, B. Li, C.L. Zhang, L.F. Cui, S.F. Kang, X. Li, L.H. Zhou, *Appl. Catal. B: Environ.* 130–131 (2013) 277–284.
- [41] M.S.P. Francisco, V.R. Mastelaro, P.A.P. Nascente, A.O. Florentino, *J. Phys. Chem. B* 105 (2001) 10515–10522.
- [42] A.E. Nelson, K.H. Schulz, *Appl. Surf. Sci.* 210 (2003) 206–221.
- [43] D.A. Peña, B.S. Uphade, P.G. Smirniotis, *J. Catal.* 221 (2004) 421–431.
- [44] T.T. Gu, R.B. Jin, Y. Liu, H.F. Liu, X.L. Weng, Z.B. Wu, *Appl. Catal. B: Environ.* 129 (2013) 30–38.
- [45] M.A. Larrubia, G. Ramis, G. Busca, *Appl. Catal. B: Environ.* 30 (2001) 101–110.
- [46] L. Chen, J.H. Li, M.F. Ge, *Environ. Sci. Technol.* 44 (2010) 9590–9596.
- [47] K.I. Hadjiivanov, *Catal. Rev.* 42 (2000) 71–144.
- [48] A. Łamacz, A. Krztoń, G. Djéga-Mariadassou, *Appl. Catal. B: Environ.* 142–143 (2013) 268–277.
- [49] S. Brandenberger, O. Kröcher, A. Tissler, R. Althoff, *Catal. Rev.* 50 (2008) 492–531.